



# Evaluation of silicon membranes for extracorporeal membrane oxygenation (ECMO)

Emily N. Abada<sup>1</sup> · Benjamin J. Feinberg<sup>1</sup> · Shuvo Roy<sup>1</sup>

Published online: 5 October 2018  
© Springer Science+Business Media, LLC, part of Springer Nature 2018

## Abstract

While extracorporeal membrane oxygenation (ECMO) is a valuable therapy for patients with lung or heart failure, clinical use of ECMO remains limited due to hemocompatibility concerns with pro-coagulatory hollow fiber membrane geometries. Previously, we demonstrated the feasibility of silicon nanopore (SNM) and micropore ( $S\mu\text{M}$ ) membranes for transport between two liquid-phase compartments in blood-contacting devices. Herein, we investigate various pore sizes of SNM and  $S\mu\text{M}$  membranes – alone or with a polydimethylsiloxane (PDMS) protective coating – for parameters that determine suitability for gas exchange. We characterized the bubble or rupture point of these membranes to determine sweep gas pressures at which gas emboli would form. The smallest pore size SNM and the  $S\mu\text{M}$  with PDMS coating could be pressurized in excess of 260 cmHg without rupture, which is comparable to hollow fiber sweep gas pressures. Oxygen flux for the  $S\mu\text{M}$  with and without PDMS was insignificantly different at  $0.0306 \pm 0.0028$  and  $0.0297 \pm 0.0012$  mL/min, respectively, while SNM flux was significantly lower at  $0.0149 \pm 0.0040$  mL/min. However, the area-normalized mass transfer coefficient of the SNM was  $338 \pm 54$  mL  $\text{O}_2$   $\text{m}^{-2}$   $\text{min}^{-1}$   $\text{cmHg}^{-1}$  – an order of magnitude higher than that of the  $S\mu\text{M}$  with and without PDMS ( $57.3 \pm 5.5$  and  $55.6 \pm 2.2$  mL  $\text{O}_2$   $\text{m}^{-2}$   $\text{min}^{-1}$   $\text{cmHg}^{-1}$ ). Ultimately, we conclude that  $S\mu\text{M}$ -PDMS may make effective membranes for ECMO, since they are both mechanically robust and capable of high oxygen flux.

**Keywords** Extracorporeal membrane oxygenation · ECMO · MEMS · Silicon membrane · Bubble point · PDMS

## 1 Introduction

Extracorporeal membrane oxygenation (ECMO) is a clinical alternative to mechanical ventilation by which oxygen is delivered to the blood and carbon dioxide is removed. Since its initial development, ECMO has become a well-established treatment that is used on nearly 8000 neonatal, pediatric, and adult patients annually worldwide (Peek et al. 2006; Thiagarajan et al. 2017; Yeager and Roy 2017). Despite ECMO's effectiveness as a treatment, its use remains limited due to its high risk profile (Vaquer et al. 2017). The large membrane area and tortuous blood flow path around the hollow fibers can cause blood clotting within the circuit; in turn, the high systemic anticoagulation prescribed to prevent these clots can cause

devastating bleeding. Clotting and bleeding are the most common causes of complications in patients, pointing to the need for a smaller, more efficient ECMO system with reduced dependence on high systemic anticoagulation (Brown and Goldman 2008; Gaffney et al. 2010).

Advances in microelectromechanical systems (MEMS) technology may be able to address the deficiencies of hollow fiber membranes through innovative approaches to high flux gas exchange membranes, and overall device design (Potkay 2014). Past work in our lab has developed silicon nanopore membranes (SNM) for use in blood-contacting devices (Fissell et al. 2009; Kanani et al. 2010; Kim et al. 2016; Song et al. 2017). Since then, we have expanded this concept to include membranes with larger, micron-scale pores employed for gas transport applications (Dharia et al. 2017; Yeager 2017). One potential disadvantage of these silicon micropore membranes ( $S\mu\text{M}$ ) is that they are far more susceptible to transmembrane leakage of gas bubbles or blood plasma compared to the smaller pore SNM. To address this potential limitation of  $S\mu\text{M}$ , we have developed a method of applying a solid layer of polydimethylsiloxane (PDMS) to the surface of the  $S\mu\text{M}$  – an adaptation derived from PDMS microfluidic

✉ Emily N. Abada  
shuvo.roy@ucsf.edu

<sup>1</sup> Department of Bioengineering and Therapeutic Sciences, University of California, 1700 4th St, QB3 Byers Hall Rm 203A, San Francisco, CA 94158, USA

oxygenators (Dharia et al. 2017). PDMS is highly permeable to both oxygen and carbon dioxide, making it capable of facilitating respiratory gas exchange. With the combination of the silicon membrane and PDMS layer, the composite “S $\mu$ M-PDMS” is imbued with several possible advantages, whereby the silicon membrane mechanically reinforces the PDMS while preventing transmembrane leakage.

The purpose of this work is to examine the effect of SNM and S $\mu$ M design on pressure resilience and maximum gas flux. An ideal ECMO membrane would be robust enough to withstand high sweep gas pressures, which would lead to a greater pressure gradient that would drive oxygen into the blood. SNM and S $\mu$ M may have different advantages when considered as potential ECMO membranes: the SNM can withstand higher sweep pressures with a smaller pore size, while the higher pore area of the S $\mu$ M may yield a higher oxygen flux. As such, both types of silicon membranes were evaluated for the effects of pore size, pore area, and distribution on maximum gas pressure prior to gas bubble formation. Subsequently, the most robust membranes were examined for gas transport efficiency, which would determine the final suitability of the silicon membranes for ECMO applications.

## 2 Materials and methods

### 2.1 Membrane fabrication

Following prior work in this lab, the SNM and S $\mu$ M were created with a uniform pore distribution and high level of pattern fidelity (Dharia et al. 2017; Fissell et al. 2009; Kim et al. 2016). Briefly, SNM are created from a silicon wafer starting with thermal oxidation growth of SiO<sub>2</sub> followed by low pressure chemical vapor deposition (LPCVD) of polysilicon, which is then patterned through dry etching (Fig. 1). Controlled, tunable growth of another layer of sacrificial SiO<sub>2</sub> on top of this polysilicon defines the width of the future pores in the membrane. An anchor layer is then patterned through wet etching. A second layer of polysilicon is

deposited with LPCVD flush with the existing layers, followed with a blanket etch of the polysilicon until the sacrificial oxide is exposed. The SNM are then protected with deposited low temperature oxide, and original silicon wafer is etched away through deep reactive ion etching (DRIE) to expose the sacrificial oxide on both sides. Finally, the oxide is etched away in a wet etching process to yield the nanometer-scale pores. S $\mu$ M are manufactured with a simpler process, in which the pores are directly patterned into a single layer of polysilicon on top of silicon oxide (Fig. 2a–d). The initial oxide only is etched away to create the pores. Pore sizes for SNM were intended to be 11, 30, and 40 nm as defined by oxide thickness, while S $\mu$ M pores were intended to be 500 and 1000 nm as defined by the lithography step.

To create S $\mu$ M-PDMS, a 5  $\mu$ m-thick layer of PDMS is made using a multistep sacrificial layer method, and then applied to the surfaces of the S $\mu$ M via O<sub>2</sub> plasma bonding (Fig. 2e–g). A  $\sim$ 300  $\mu$ m layer of Sylgard 184 PDMS (Dow Corning: 4019862) is mixed at a 10:1 monomer-to-crosslinker ratio, spin coated onto a silicon wafer, and then cured for 2 h in an 80 °C oven. After a brief oxygen plasma treatment to make the surface wettable (Harrick Plasma PDC-001, Harrick Plasma, Ithaca, NY USA), a 5% w/w solution of polyvinyl alcohol in water is spin coated on top of the first PDMS layer and cured for 1 h at 60 °C (Sigma Aldrich: P8136-250G). Finally, mixed Sylgard 184 is diluted with hexanes (Sigma Aldrich: 227064-1 L) at a 1:1 ratio, spin coated on top of the PVA to a thickness of  $\sim$ 5  $\mu$ m, and cured at 80 °C for 2 h. The cured PDMS is cut from the wafer into strips, and placed into the plasma oven along with the S $\mu$ M. Following plasma treatment, the S $\mu$ M are briefly dipped into DI water, and the strips of PDMS are placed face down on top of the membranes such that the 5  $\mu$ m PDMS layer is in contact with the polysilicon face of the membrane. The plasma bond is strengthened with 70 °C heat and pressure to ensure even contact. After 12 h of bonding, the excess PDMS is cut from the membrane and the membranes are allowed to soak in 70 °C DI water until the PVA layer completely dissolves creating the S $\mu$ M-PDMS membrane.

**Fig. 1** Fabrication of SNM membranes. Step (c) shows the deposition of sacrificial oxide to form pores, which is removed through wet etching in step (e)

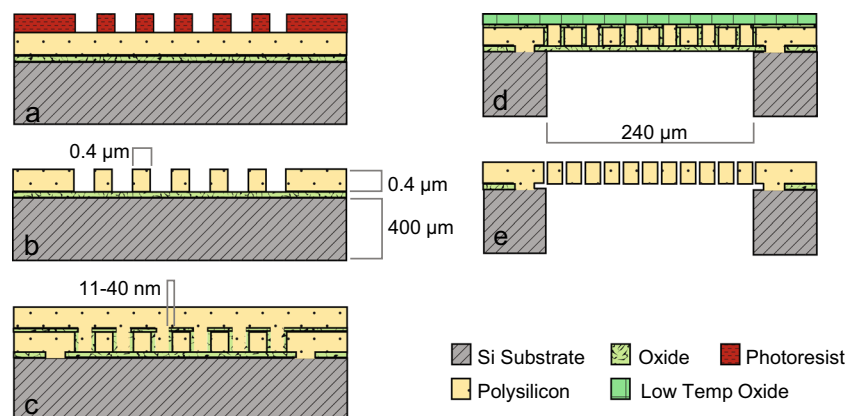
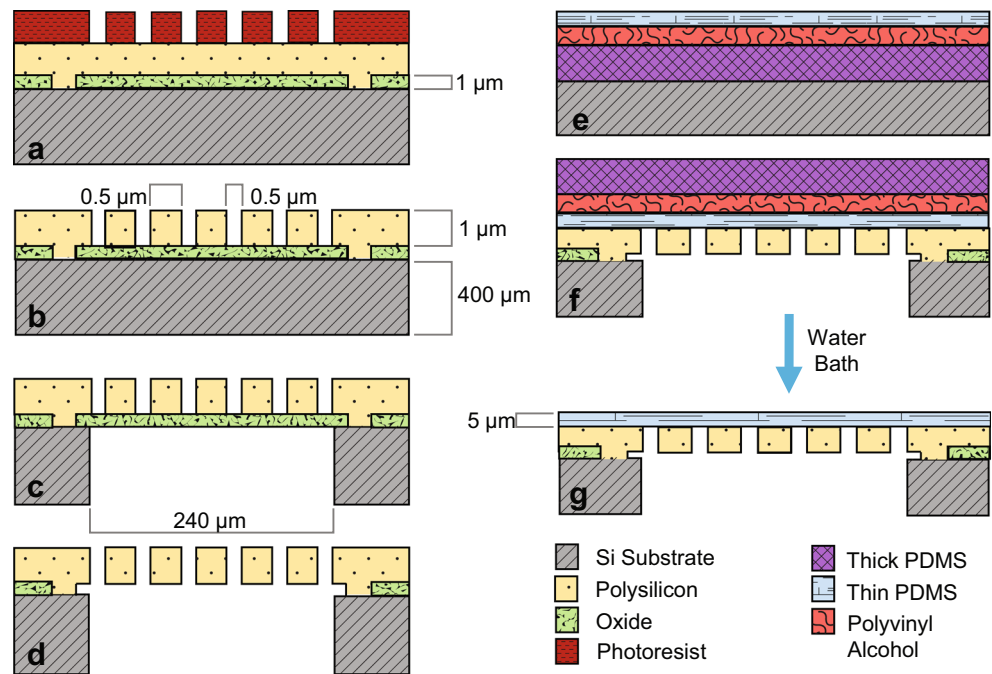


**Fig. 2** Fabrication of S $\mu$ M (a–d), and application of PDMS (e–g) to form S $\mu$ M-PDMS. Adapted from Dharia et al. (2017)



Pore widths were validated through hydraulic permeability testing and SEM imaging of membranes. Hydraulic permeability testing was performed on SNM after wet etching of the pores (Smith et al. 2011). By establishing a ~5 cmHg pressure gradient of water across the membrane, the volume flow rate of the permeate from the membrane could be measured through timed collection. From the following equation, the actual pore width of the membrane could be related to the permeate flow rate, pressure drop, and other length dimensions of the pore:

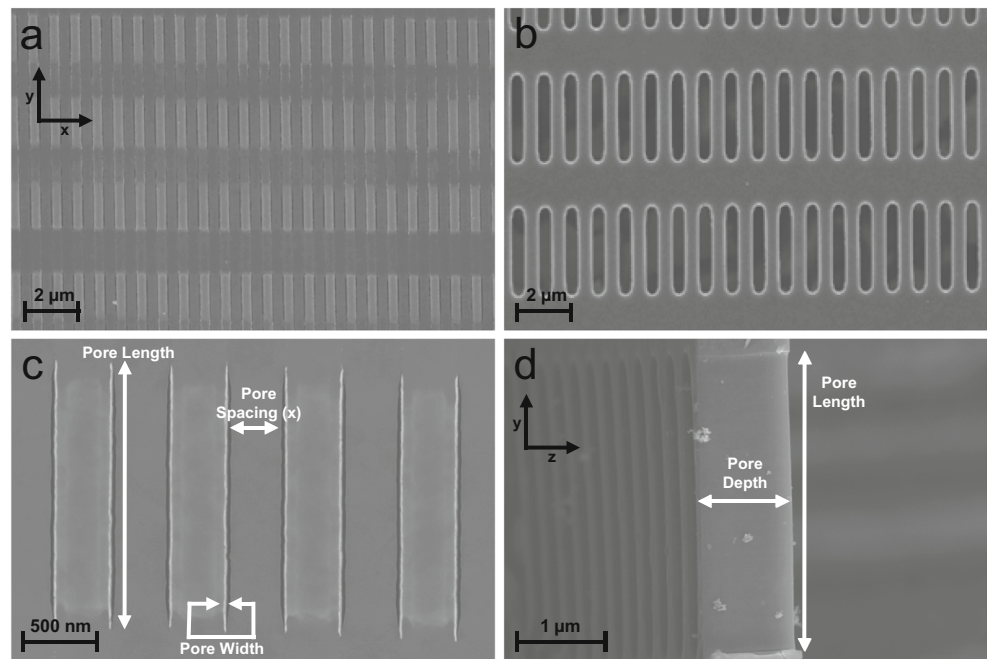
$$w = \left( \frac{12\mu h \Delta Q_{perm}}{L \Delta P} \right)^{1/3} \tag{1}$$

All variables and constants for transport equations can be found in Table 1. Hydraulic permeability testing showed that the SNM had pore sizes of  $10.2 \pm 0.6$ ,  $22.3 \pm 3.4$ , and  $33.0 \pm 3.1$  nm. The measured pore sizes indicated that the SNM were patent, and that the pore sizes were on the same order of magnitude as intended. Since the pores of the S $\mu$ M were large enough to be easily visualized, light microscopy was used to measure the size of S $\mu$ M pores (Leica DM4000M, Leica Microsystems, Buffalo Grove, IL USA), and hydraulic permeability testing was unnecessary. SEM imaging was used to confirm the pore widths of SNM and S $\mu$ M, and the thickness of the PDMS layer of the S $\mu$ M-PDMS was determined to be ~5  $\mu$ m (Fig. 3 and Table 2).

**Table 1** List of variables and constants for membrane transport equations

| Variable                                  | Units   |                  |
|---|---|------------------|
| Pore width (w)                            | m   |                  |
| Pore length (L)                           | m   |                  |
| Pore depth (h, $\delta_m$ )               | m   |                  |
| Membrane area ( $A_m$ )                   | m <sup>2</sup>  |                  |
| Pressure (P)                              | cmHg  |                  |
| Flow rate (Q)                             | m <sup>3</sup> s <sup>-1</sup>  |                  |
| Bubble point shape factor ( $\kappa$ )    | –   |                  |
| Hydraulic diameter ( $D_H$ )              | m   |                  |
| Flux (J)                                  | mL O <sub>2,STP</sub> min <sup>-1</sup>   |                  |
| Total mass transfer coefficient ( $k_T$ ) | cm O <sub>2,STP</sub> <sup>3</sup> m <sup>-2</sup> min <sup>-1</sup> cmHg <sup>-1</sup> |                  |
| Permeability ( $P_m$ )                    | mol O <sub>2</sub> m <sup>-1</sup> min <sup>-1</sup> cmHg <sup>-1</sup>                 |                  |
| Constants                                 | Units   | Value            |
| Surface tension – Water/Air ( $\sigma$ )  | mN/m  | 72.75            |
| Contact angle – Water on Si ( $\theta$ )  | Degrees   | 40               |
| Density of oxygen ( $\rho_{STP}$ )        | kg m <sup>-3</sup>  | 1.429            |
| Henry's law constant (H)                  | mol H <sub>2</sub> O · atm O <sub>2</sub> /mol O <sub>2</sub>                           | $4.2 \cdot 10^4$ |
| Molar concentration of water ( $c_L$ )    | mol/L   | 55.5             |

**Fig. 3** SEM images of membranes. (a) and (b) are 1.82 k magnification plan view images of 30 nm and 500 nm pore membranes, respectively. (c) is a 25 k magnification plan view image of a 30 nm-pore wide membrane with dimensions labeled. (d) is a cross sectional image of a 500 nm pore membrane showing pore depth



## 2.2 Failure point testing

The failure point of the membranes was investigated to determine the maximum sweep gas pressure that the membranes could support prior to gas bubble formation in liquid. Failure point can be further characterized as either bubble point or rupture point, depending on the cause of the bubble formation. Bubble point is defined as the gas pressure at which the largest pore of a wetted membrane will become completely de-wetted, leading to gas bubbles on the liquid side of the membrane. Rupture point is the pressure at which the membrane will break due to the mechanical strain arising from the deflections upon application of gas pressure, causing gas bubbles to traverse the membrane. Unlike rupture point, which is an irreversible and non-repeatable measurement, bubble point testing is both reversible and consistent because the membrane remains intact upon completion of the test. Silicon membranes with smaller pores will require higher gas pressure to de-wet

and reach bubble point than those with larger pores. Ultimately, they may reach their rupture pressure before they reach their bubble point.

For this study, a selection of membranes was used with pore sizes ranging from approximately 10 nm to 1  $\mu\text{m}$ , and classified as either SNM (pore size < 100 nm) or  $\text{S}\mu\text{M}$  (pore size > 500 nm). To visually measure bubble or rupture point, SNM and  $\text{S}\mu\text{M}$  were diced into 1  $\times$  1 cm square membranes, completely wetted with water, and mounted inside of a gasket-sealed transparent acrylic flow cell (Fig. 4). One side of the membrane was exposed to circulating deionized water at a flow rate of 1 mL/min, allowing visualization of gas bubbles in the liquid. The opposite side of the membrane was connected upstream to an air-filled syringe pump (kdScientific Gemini 88, Holliston, MA USA) and a pressure gauge (Druck DPI 104, General Electric, Billerica, MA USA); air flow was blocked downstream of the flow cell. The side of the membrane with the polysilicon pores was oriented to face

**Table 2** Dimensions of SNM and  $\text{S}\mu\text{M}$  as measured by SEM

| Dimensions                         | Nanopore Membranes (SNM) |            |            | Micropore Membranes ( $\text{S}\mu\text{M}$ ) |            |
|------------------------------------|--------------------------|------------|------------|---|------------|
|                                    |                          |            |            |   |            |
| Pore width (nm)                    | 10.4                     | 29.0       | 39.1       | 600.8   | 1027.0     |
| Pore length ( $\mu\text{m}$ )      | 2.17                     | 1.83       | 1.92       | .46   | 3.45       |
| Pore depth (nm)                    | 400                      | 400        | 400        | 1000  | 1000       |
| Pore spacing (nm)                  | 386                      | 368        | 362        | 400   | 468.9      |
| Pores per membrane                 | 1.56E + 07               | 1.56E + 07 | 1.56E + 07 | 3.16E + 06                                    | 2.10E + 06 |
| Pore area ( $\text{m}^2$ )         | 3.60E-07                 | 7.02E-07   | 9.36E-07   | 5.53E-06                                      | 7.36E-06   |
| Membrane area ( $\text{m}^2$ )     | 1.91E-05                 | 1.91E-05   | 1.91E-05   | 1.48E-05                                      | 1.48E-05   |
| Porosity (Pore area/Membrane area) | 1.89%                    | 3.67%      | 4.90%      | 37.33%  | 49.68%     |

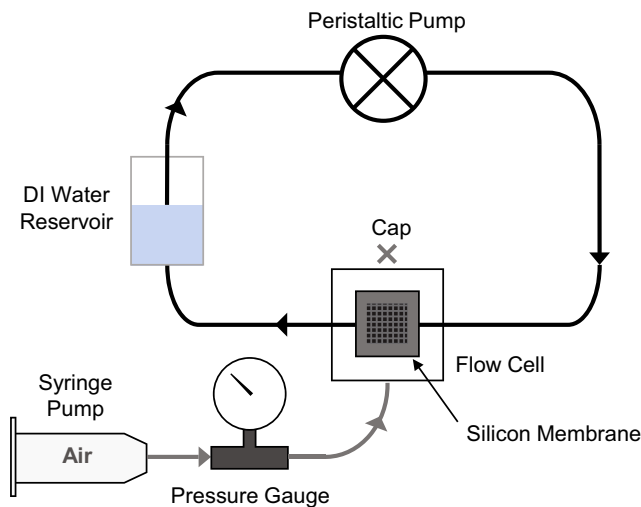


**Fig. 4** Diagram of bubble/rupture point testing setup. The membrane in the flow cell is shown with bubbles traversing the membrane as bubble or rupture point has been reached

the water to mimic the configuration of membranes when in contact with blood. Measurements of bubble point gas pressure (cmHg) were taken by pressurizing the air using the syringe pump until bubbles were observed in the liquid. Each membrane was re-tested upon completion of the first test to determine if the membrane had ruptured or had reached a repeatable bubble point. A ruptured membrane would permit bubbles at very low gas pressures – significantly lower than during the first test – while a membrane that reached its bubble point would become pressurized to the same level as the initial test.

The bubble point of any membrane can be described by the following equation:

$$\Delta P = \frac{4\sigma \cdot \cos(\theta) \cdot \kappa}{D_H} \tag{2}$$

where  $\kappa$  is an empirical, unitless “shape factor” constant that applies to non-cylindrical pore membranes and  $\Delta P$  has units of Pa (Zeman 1992). Given that hydraulic diameter is inversely proportional to bubble point pressure, membranes with larger pore sizes will reach bubble point with less pressure than membranes with smaller pores.

### 2.3 Oxygen flux and permeability *in vitro*

Following bubble/rupture point testing, SNM and S $\mu$ M that withstood the highest gas pressure without gas emboli were chosen for subsequent experiments. These membranes were assessed for their gas permeability at a constant, low pressure below the bubble/rupture point of all membranes (Fig. 5). The SNM and S $\mu$ M membranes were diced to a size of 1 cm  $\times$  6.5 cm, thoroughly dried, and mounted into a gasket-sealed polyether ether ketone (PEEK) flow cell with a channel height of 200  $\mu$ m. For gas permeability testing, the membranes were

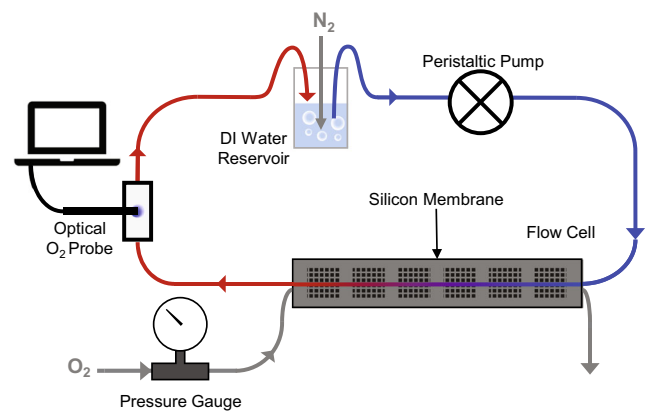


**Fig. 5** Schematic of *in vitro* oxygen permeability testing setup. Water is shown as blue when deoxygenated, and red when oxygenated after contact with the silicon membrane

diced larger than for the bubble point testing in order to ensure adequate gross gas transport. For this test, the face of the membrane with polysilicon pores was exposed to circulating, nitrogen-sparged water at a rate of 10 mL/min and hydrostatic pressure of under 5.17 cmHg, and the backside was exposed to pressurized pure oxygen sweep gas. In this experiment, the gas flow was not blocked downstream of the flow cell, but instead permitted to flow completely through. An optical oxygen probe (NeoFoxGT with FOSPOR probe, Ocean Optics, Dunedin, FL, USA) was placed downstream of the flow cell on the liquid side to detect oxygen transport across the membrane. The gas pressure of the oxygen sweep gas was raised to 26 cmHg, and oxygen flux into the water was measured by the probe. Flux ( $J$ , mL O<sub>2</sub>/min) was determined using the measured oxygen concentration in  $\mu$ mol/L before and after adding oxygen to the circuit ( $[O_2]_i$  and  $[O_2]_f$ , respectively), with a conversion of 22.4 L O<sub>2</sub>/mol at STP:

$$J = \left( [O_2]_f - [O_2]_i \right) \cdot 10^{-6} \frac{\text{mol}}{\mu\text{mol}} \cdot 22.4 \frac{\text{L}}{\text{mol}} \cdot Q \tag{3}$$

$Q$  is the flow rate of water in mL/min. From the flux, the coupled mass transfer coefficient ( $k_T$ , mL O<sub>2</sub> min<sup>-1</sup> m<sup>-2</sup> cmHg<sup>-1</sup>) was determined to represent the total transport efficiency of oxygen through the sweep gas, the membrane, and the liquid. To obtain this value, the flux from Eq. 3 is normalized by the total pressure driving force between the gas and liquid ( $\Delta P_{gas-liquid}$ , cmHg), as well as the membrane area ( $A_m$ , m<sup>2</sup>):

$$k_T = \frac{J}{\Delta P_{gas-liquid} \cdot A_m} \tag{4}$$

For the calculations in this study, the membrane area was taken to be the total area of open pores on the membrane. The mass transfer coefficient can be further broken down into its measurable parameters, where  $P_{O_2,gas}$  is the gas driving

pressure (cmHg) and  $P_{O_2,H_2O}$  is the partial pressure of oxygen in the water measured using the oxygen probe (cmHg):

$$k_T = \frac{\Delta[O_2] \cdot Q}{\left( P_{O_2,gas} - \frac{P_{O_2,H_2O,f} - P_{O_2,H_2O,i}}{2} \right) \cdot A_m} \quad (5)$$

Both the oxygen flux and mass transfer coefficient can be used to aid our understanding of the influence of membrane design on gas transfer, and thereby, help determine if silicon membranes are suitable for ECMO.

### 3 Results and discussion

#### 3.1 Failure point testing

Failure point data for the SNM, S $\mu$ M, and S $\mu$ M-PDMS are shown in Table 3 and Fig. 6. The S $\mu$ M without PDMS showed bubble points at approximately 84.1 cmHg for 500 nm pores, and 43.9 cmHg for 1000 nm. These bubble points were found to be repeatable, indicating that the micropore membranes had not ruptured. The smaller pore S $\mu$ M had a higher bubble point than the larger pore membrane, which is consistent with Eq. 2. While the SNM without PDMS produced identifiable bubble points, the S $\mu$ M-PDMS showed no membrane rupture or bubbles during the course of the test. Instead, the membranes did not rupture prior to the maximum gas pressure permitted by the syringe pump testing system – approximately 260 cmHg.

The two SNM with relatively larger pore sizes ruptured at pressures of 220 cmHg and 170 cmHg for membranes with 30 and 40 nm pores, respectively. This rupture point was the result of the membranes breaking while under pressure, which was verified through light microscopy. The 40 nm pore SNM ruptured at a lower pressure than the 30 nm pore SNM likely due to the fact that the larger pore membrane was reinforced with less additional silicon than the smaller-pore counterpart. The SNM with the smallest pores (~11 nm) did not rupture or reach bubble point before the syringe pump system reached its maximum pressure. Ultimately, the two types of membranes with the highest bubble/rupture points were the S $\mu$ M-PDMS, and the 11 nm pore size SNM. These membranes were able to resist rupture before the conclusion of the test, indicating that they would be able to withstand greater than ~260 cmHg of

pressure prior to the formation of gas emboli in blood. This pressure is comparable to that of existing hollow fiber oxygenators, which can be used at pressures up to 260 cmHg (50 psi) clinically (Alexander et al. 2014; Morley et al. 2013). Microfluidic, PDMS-based oxygenators are comparatively used at sweep gas pressures of 16 cmHg or lower to prevent rupture (Potkay 2013). For example, Potkay et al. (2011) used a sweep gas pressure of 16.0 cmHg, while Hoganson et al. (2010) and Kung et al. (2008) used lower pressures of 0.475 cmHg and 1–2 cmH<sub>2</sub>O, respectively (Hoganson et al. 2010; Kung et al. 2008; Potkay et al. 2011).

#### 3.2 Oxygen flux and permeability *in vitro*

From the initial set of membrane types, the S $\mu$ M-PDMS and 11 nm pore SNM were selected for further testing to determine oxygen flux through each membrane, since they were able to resist failure prior to the end of the test. Since one of the membrane types selected was the S $\mu$ M-PDMS, an additional group of 500 nm pore S $\mu$ M without PDMS was also tested for gas permeability. It was essential to compare the transport of the S $\mu$ M with and without PDMS to determine if the PDMS layer had a significant impact on gas transport. Gas permeability testing was conducted for all chips at a sweep gas pressure below the failure point of all membranes (26 cmHg) to achieve comparative tests of gas flux.

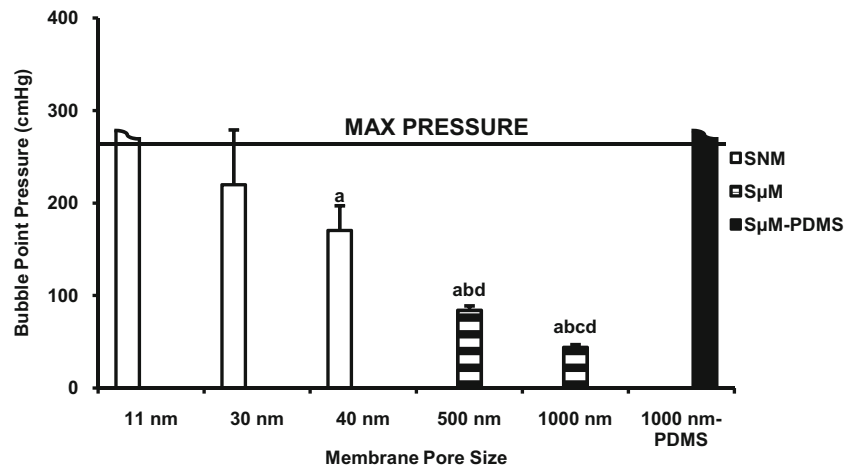
The oxygen flux from each membrane (using Eq. 3) is shown in Fig. 7a. Based on Eq. 5, the coupled mass transfer coefficient was also determined for each membrane, taking the area to be the area of open pores on the membranes (Fig. 7b). The PDMS coated membranes produced the most oxygen flux at 0.03 mL/min. As can be seen in Fig. 7a, the oxygen flux from the S $\mu$ M with and without PDMS are indistinguishable and  $k_T$  values for both membranes were also insignificantly different. The PDMS layer, therefore, provides little resistance to oxygen transport. Compared to the S $\mu$ M, the SNM showed significantly lower oxygen flux – only 40% of the S $\mu$ M flux. Higher transport through the S $\mu$ M is likely due to the significantly greater open pore area of S $\mu$ M compared to the SNM. However, the mass transfer coefficient of the SNM when normalized by actual pore area is significantly higher by an order of magnitude. This result would indicate that, per pore, more transport is exhibited by the smaller pore membranes –

**Table 3** Failure points of nanopore and micropore membranes. The 11 nm pore SNM and 1000 nm pore S $\mu$ M with PDMS both exceeded the maximum pressure of the syringe pump without bubbling or

rupturing. Maximum pressure of the syringe pump was somewhat variable due to inconsistent syringe pump performance, leading to differences between the membrane maximum pressures

| Pore Size (nm)       | 11               | 30                   | 40                   | 500                  | 1000                 | 1000 + PDMS      |
|----------------------|------------------|----------------------|----------------------|----------------------|----------------------|------------------|
| Failure Point (cmHg) | 310 ± 67.4 (MAX) | 220 ± 59.5 (rupture) | 170 ± 26.7 (rupture) | 84.1 ± 4.95 (bubble) | 43.9 ± 2.99 (bubble) | 276 ± 65.6 (MAX) |

**Fig. 6** Bubble or rupture points of silicon membranes related to pore size. Significant difference ( $p < 0.05$ ) is indicated above chart bars: difference from from 11 nm SNM shown by (a), 30 nm shown by (b), 40 nm shown by (c), and 1000 nm-PDMS membrane. Maximum pressure indicated by dashed line



pointing to a nonlinear relationship between pore area and gas flux (Fissell et al. 2011). Despite the higher transport per pore of the SNM, compared to the SµM, overall more gas transport was generated when using membranes of higher porosity.

From the analytical modeling described for this testing system in Dharia et al. (2017), the total coupled mass transfer coefficient can be related to mass transfer through the membrane and the liquid:

$$\frac{1}{k_T} = \frac{\delta_m}{P_m \cdot \rho_{STP}} + \frac{H}{c_L \cdot k_{O_2, H_2O}} \tag{6}$$

The first entity in this equation represents transport through the membrane itself:  $\delta_m$  is membrane thickness (m),  $P_m$  represents membrane permeability (cmSTP3cm cm<sup>-1</sup> min<sup>-1</sup> cmHg<sup>-1</sup>), and  $\rho_{STP}$  is the density of oxygen at standard temperature and pressure (mol/m<sup>3</sup>). The second part represents transport through of gas through the liquid phase of the system: H is the Henry’s Law Constant,  $c_L$  is the molar concentration of water. When using silicon membranes for gas-into-liquid transport, it can be assumed that transport within the gas regime is instantaneous, and contributes little to transport resistance. By

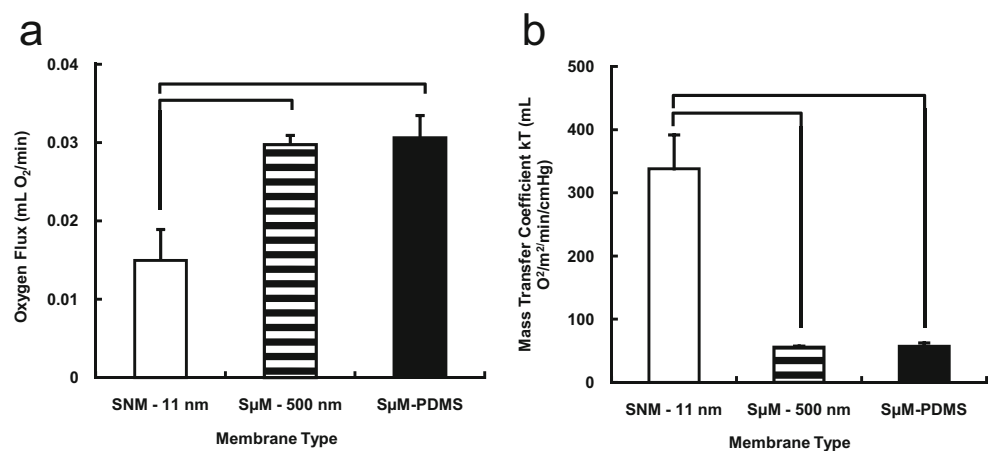
extension, transport through the silicon membrane can also be assumed instantaneous since the pores are filled with gas, reducing the mass transfer coefficient to:

$$\frac{1}{k_T} = \frac{H}{c_L \cdot k_{O_2, H_2O}} \tag{7}$$

Essentially, this reduction leaves liquid phase as the largest determinant of transport in this regime, although the amount of open membrane area dictates how much of the membrane contributes to transport.

Considering the importance of the liquid phase to overall gas transport, we speculate that the high area-normalized transport in SNM is due to phenomena within the liquid phase boundary layer. As oxygen gas exits the membrane, it enters a microns thick boundary layer that collects oxygen near the surface before it can diffuse into the liquid bulk. Within the boundary layer, the pores of both SNM and SµM behave as point/area sources for oxygen, which can diffuse outwards laterally into the spaces between pores. The effect of this lateral diffusion implies the membranes yield a higher oxygen flux than the pore area alone would suggest, creating a

**Fig. 7** Plots of (a) oxygen flux and (b) pore area-normalized mass transfer coefficient from silicon membranes downselected from bubble point experiments. Bars above chart indicate significant difference by one way ANOVA ( $p < 0.05$ )



nonlinear relationship between open pore area and oxygen flux. In  $S_{\mu\text{M}}$ , pore size and pore spacing are of similar magnitude, and the additive effect of the boundary layer lateral diffusion is likely minimal when flux is normalized by pore area. Comparatively, the pores of SNM are far smaller than the spacing between pores, and contribution of this accumulated oxygen to overall flux is far more evident than for the  $S_{\mu\text{M}}$ . The effect of this nonlinear relationship drives the transport of SNM to appear higher when normalized by open pore area, since the pores comprise such a small fraction of the overall membrane surface area. However, the accumulated oxygen in the boundary layer of the SNM is not sufficient to outdo the advantage of the overall open pore area of the current  $S_{\mu\text{M}}$ .

From the  $S_{\mu\text{M}}$ -PDMS flux data, the oxygen transport rates of the membranes were found to be 0.03 mL  $\text{O}_2/\text{min}$ , with a membrane area of  $6.5\text{e-}4\text{ m}^2$  at a 10 mL/min liquid flow rate. Although the device conditions of this study were not optimized for scale up, it is possible to use this transport data to determine the operating conditions of a theoretical full-scale oxygenator. To oxygenate a 3.5 kg neonate with an oxygen requirement of 6 mL/kg/min, a total of 700 membranes would be needed with a membrane area of  $0.455\text{ m}^2$ . This surface area is similar to that of the Maquet QUADROX-i Neonatal ( $0.38\text{ m}^2$ ), and could be reduced with fabrication of more porous membranes. However, at the flow rate used in this study, a scaled up device with 700 membranes and  $0.455\text{ m}^2$  of area would be capable of 7 L/min of blood flow, which far exceeds the 0.35 L/min cardiac output of a neonate. Ultimately, a future  $S_{\mu\text{M}}$  ECMO device will require optimization of the device design to fully scale the flow rate and oxygen transport to match patient requirements.

One drawback of this study is the limited range of pore sizes of membranes available. Between the SNM and  $S_{\mu\text{M}}$ , there is an unaddressed transitional range of 50–500 nm pores. It is possible that a membrane with pores in the transitional range would be better suited to meet bubble point and gas flux metrics than either the SNM or  $S_{\mu\text{M}}$ . A membrane with pores between 100 and 500 nm may have a higher bubble point than the current  $S_{\mu\text{M}}$  for more pressure resistance, while also retaining the higher pore area of the  $S_{\mu\text{M}}$  for more gas flux.

## 4 Conclusion

This study demonstrates that silicon membranes can be used with high sweep gas pressures and yield high-efficiency oxygenation *in vitro*, opening up possibilities for use as ECMO membranes. The highest gas transfer and rupture resistance was seen with the  $S_{\mu\text{M}}$  coated with PDMS, making this type of membrane the most suitable silicon membrane for ECMO.

Subsequent research on device design would be required to scale the membranes to meet clinical oxygenation needs. Further optimization of the device design would be needed to establish the effects of channel height, liquid flow rate, and membrane pore distribution on oxygen flux. With optimization of the device design, silicon membranes could be employed for robust, high efficiency oxygenation.

**Acknowledgements** This research was supported by the National Heart, Lung, and Blood Institute of the NIH under Grant Number U54HL119893; NIH/NCATS UCSF-CTSI Grant Number UL1 TR001872; and US FDA Grant P50 FD003793 through the UCSF Pediatric Device Consortium. The membranes used in this study were designed and fabricated by JaeHyun Park of UCSF, and flow cells were designed by Nathan Wright of UCSF.

## References

- J.V. Alexander, J.W. Neely, E.A. Grulke, J. Polym. Sci. Part B Polym. Phys. **52**, 1366 (2014)
- K.L. Brown, A.P. Goldman, Early Hum. Dev. **84**, 143 (2008)
- A. Dharia, E. Abada, B. Feinberg, T. Yeager, W. Moses, J. Park, C. Blaha, N. Wright, B. Padilla, S. Roy, Artif. Organs **42**, 166 (2017)
- W.H. Fissell, A. Dubnisheva, A.N. Eldridge, A.J. Fleischman, A.L. Zydney, S. Roy, J. Membr. Sci. **326**, 58 (2009)
- W.H. Fissell, A.T. Conlisk, S. Datta, J.M. Magistrelli, J.T. Glass, A.J. Fleischman, S. Roy, Microfluid. Nanofluid. **10**, 425 (2011)
- A.M. Gaffney, S.M. Wildhirt, M.J. Griffin, G.M. Annich, M.W. Radomski, Br. Med. J. **341**, c5317 (2010)
- D.M. Hoganson, J.L. Anderson, E.F. Weinberg, E.J. Swart, B.K. Orrick, J.T. Borenstein, J.P. Vacanti, J. Thorac. Cardiovasc. Surg. **140**, 990 (2010)
- D.M. Kanani, W.H. Fissell, S. Roy, A. Dubnisheva, A.L. Zydney, J. Membr. Sci. **349**, 1 (2010)
- S. Kim, B. Feinberg, R. Kant, B. Chui, K. Goldman, J. Park, W. Moses, C. Blaha, Z. Iqbal, C. Chow, N. Wright, W.H. Fissell, A. Zydney, S. Roy, PLoS One **11** (2016)
- M.C. Kung, J.K. Lee, H.H. Kung, L.F. Mockros, ASAIO J **54** 390 (2008)
- S.W. Morley, P. Bieniek, M. Rosenberg, US 8,585,968 B2 (2013)
- G.J. Peek, F. Clemens, D. Elbourne, R. Firmin, P. Hardy, C. Hibbert, H. Killer, M. Mugford, M. Thalananay, R. Tiruvoipati, A. Truesdale, A. Wilson, BMC Health Serv. Res. **13**, 163 (2006)
- J.A. Potkay, Biomed. Microdevices **15**, 397 (2013)
- J.A. Potkay, Lab Chip **14**, 4122 (2014)
- J.A. Potkay, M. Magnetta, A. Vinson, B. Cmolik, Lab Chip **11**, 2901 (2011)
- R.A. Smith, A.J. Fleischman, W.H. Fissell, C.A. Zorman, S. Roy, Meas. Sci. Technol. **22**, 45802 (2011)
- S. Song, C. Blaha, W. Moses, J. Park, N. Wright, J. Groszek, W. Fissell, S. Vartanian, A.M. Posselt, S. Roy, Lab Chip **17**, 1778 (2017)
- R.R. Thiagarajan, R.P. Barbaro, P.T. Rycus, D.M. McMullan, S.A. Conrad, J.D. Fortenberry, M.L. Paden, ASAIO J. **63**, 60 (2017)
- S. Vaquer, C. De Haro, P. Peruga, J.C. Oliva, A. Artigas, Ann. Intensive Care **7**, 51 (2017)
- T. Yeager, *High Efficiency Asymmetric Membranes for Extracorporeal Membrane Oxygenation* (University of California, San Francisco, 2017)
- T. Yeager, S. Roy, Artif. Organs **41** (2017)
- L. Zeman, J. Membr. Sci. **71**, 233 (1992)